Supplementary Information (SI) for Journal of Materials Chemistry A.

— Supporting Information —

Pivotal Role of Sb Vacancies in Quaternary Half-Heusler Thermoelectrics

Illia Serhiienko,[†,‡] Michael Parzer,[¶] Fabian Garmroudi,[¶] Andrei Novitskii,[†] Naohito Tsujii,[†] Tarachand,[†] Ernst Bauer,[¶] Yuri Grin,[§] and Takao Mori[*,†,‡]

†*Research Center for Materials Nanoarchitectonics (MANA), National Institute for Materials Science (NIMS), Tsukuba 305-0044, Japan.*

‡*Graduate School of Pure and Applied Sciences, University of Tsukuba, Tsukuba 305-8671, Japan.*

¶*Institute of Solid State Physics, TU Wien, Vienna A-1040, Austria.*

§*Max Planck Institute for Chemical Physics of Solids, Dresden 01187, Germany*

E-mail: MORI.Takao@nims.go.jp

Phase Formation Mechanism

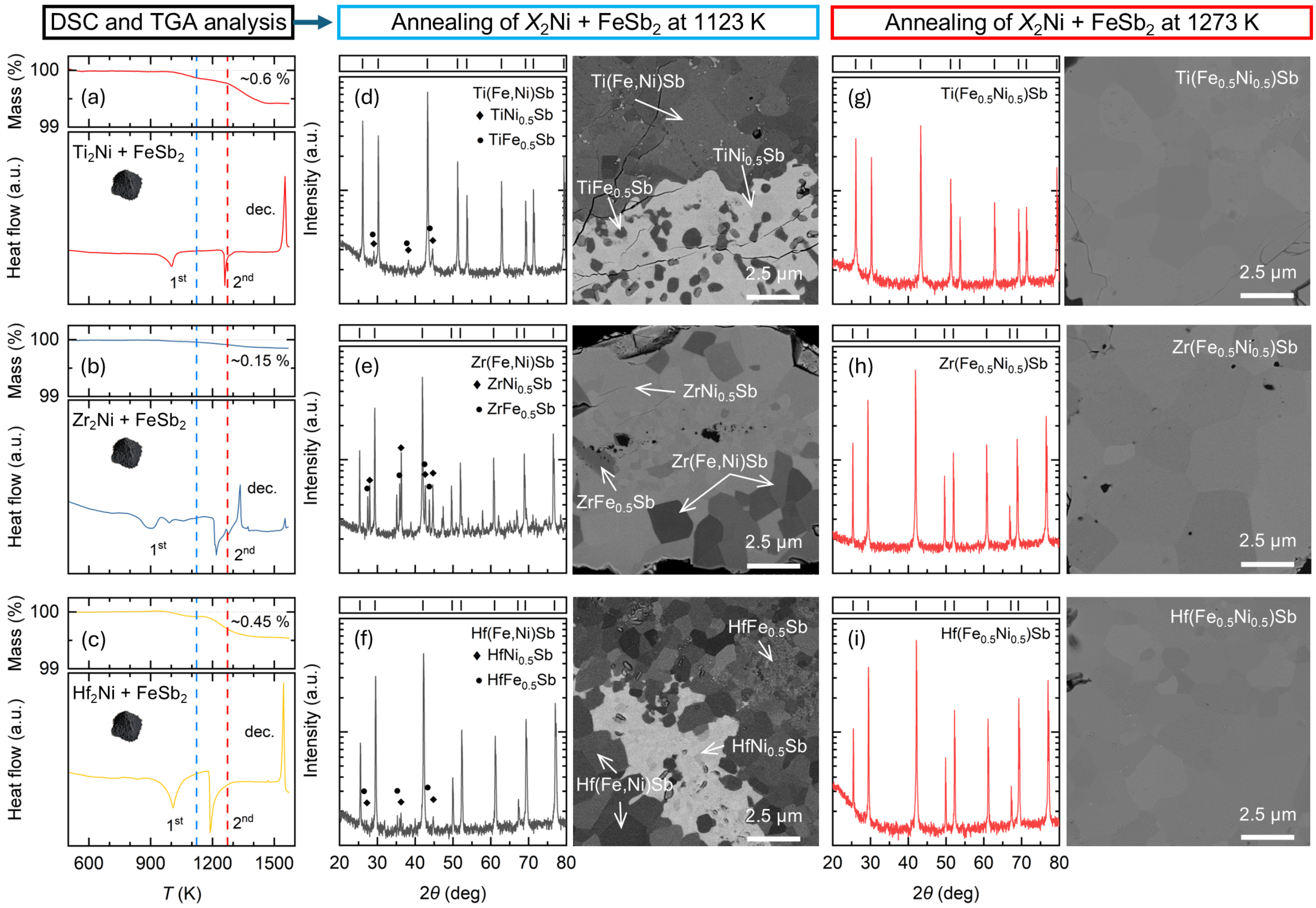

Figure S1: Differential scanning calorimetry (DSC), thermogravimetric analysis (TGA), X-ray diffraction (XRD), and scanning electron microscopy (SEM) of X_2Ni (X = Ti, Zr, Hf) and FeSb$_2$ powder mixtures. (a-c) Mass loss (top panels) and heat flow (bottom panels) of X_2Ni (X = Ti, Zr, Hf) and FeSb$_2$ powder mixtures. The two vertical dashed lines represent the two temperatures at which the samples were annealed (blue: 1123 K, red: 1273 K) for phase formation investigation. (d-f) XRD and corresponding SEM images for X_2Ni (X = Ti, Zr, Hf) and FeSb$_2$ powder mixtures after annealing at (g)-(i) 1123 K and (g-i) 1273 K in an evacuated quartz ampoule.

X_2Ni (X= Ti, Zr or Hf) and FeSb$_2$ master alloys were mixed for 30 minutes in a shaker mill (8000D Mixer/Mill, SPEX SamplePrep, USA) to achieve homogeneous powder for further DSC and TGA analyses. Upon heating, two endothermic peaks appear at DSC curves, one ranging from 850 to 1000 K (labeled as “1$^{\text{st}}$“) and the second one ranging from 1150 to 1250 K (labeled as “2$^{\text{nd}}$“) as shown in Fig. S1a-c. To investigate the phase formation process, we separately prepared another powder mixture of X_2Ni (X= Ti, Zr or Hf) and FeSb$_2$ and annealed them in an evacuated quartz tube for 120 hours at 1123 K and 1273 K, respectively.

XRD analysis of the powder annealed at 1123 K for 3 days (Fig. S1d-f) revealed the formation of a half-Heusler phase along with $XM_{0.5}$Sb (M = Fe or Ni) secondary phases. SEM and EDX analysis of the polished powder confirmed the presence of these secondary phases and indicated that the Fe/Ni ratio within the half-Heusler phase varied significantly, resulting in a X(Fe$_{0.5-\delta}$Ni$_{0.5-\delta}$)Sb chemical composition. According to both XRD and SEM analysis, the Zr-based sample contained a higher amount of secondary phases compared to the Ti- and Hf-based samples.

Table S1: The temperatures corresponding to the peaks of the primary (1^{st}) and complete (2^{nd}) phase formation, the decomposition temperature of the half-Heusler phase, and the total mass loss at 1573 K in the $X(\mathrm{Fe}_{0.5}\mathrm{Ni}_{0.5})\mathrm{Sb}$ compounds (X = Ti, Zr, or Hf).

Property	$\mathrm{Ti(Fe_{0.5}Ni_{0.5})Sb}$	$\mathrm{Zr(Fe_{0.5}Ni_{0.5})Sb}$	$\mathrm{Hf(Fe_{0.5}Ni_{0.5})Sb}$
1^{st}, K	960	860	970
2^{nd}, K	1250	1220	1190
Decomposition, K	1570	1340	1570
Mass loss, %	0.60(1)	0.15(1)	0.45(1)

XRD analysis of the powder annealed at 1273 K for 3 days (Fig. S1g-i) showed a half-Heusler phase without any secondary phases, confirming complete phase formation. Microstructural investigations of the obtained powder uphold the XRD findings. The composition of the powder grains was stabilized, closely approximating the desired $X(\mathrm{Fe}_{0.5}\mathrm{Ni}_{0.5})\mathrm{Sb}$ composition.

Annealing the $\mathrm{Zr(Fe_{0.5}Ni_{0.5})Sb}$ sample above 1340 K led to the decomposition of the half-Heusler phase and the formation of high-temperature phases such as $\mathrm{Zr_2Sb}$ and others.

Elemental composition analysis

Specimens for EDX, ICP-OES, and Rietveld analysis were prepared from cut sections of the samples. For elemental analysis using EDX, the specimens were mirror-polished to minimize the influence of surface morphology on the measured intensities.

Table S2: Chemical composition of obtained bulk $X(\mathrm{Fe_{0.5}Ni_{0.5}})\mathrm{Sb}$ where $X = $ Ti, Zr or Hf materials delivered by EDX, ICP-OES, and Rietveld analysis of XRD patterns.

Sample	Ti	Zr	Hf	Fe	Ni	Sb
$\mathrm{Ti(Fe_{0.5}Ni_{0.5})Sb}$						
Nominal, at.%	33.3	0	0	16.7	16.7	33.3
EDX, at.%	33.3	0	0	16.7	16.7	33.3
ICP, at.%	33.39	0	0	16.81	16.70	32.89
Rietveld, at.%	33.3	-	-	33.3		32.89
an $\mathrm{Ti(Fe_{0.5}Ni_{0.5})Sb}$						
Nominal, at.%	33.3	0	0	16.7	16.7	33.3
EDX, at.%	33.3	0	0	16.7	16.7	33.0
ICP, at.%	33.43	0	0	16.87	16.79	32.52
Rietveld, at.%	33.3	-	-	33.3		31.9
$\mathrm{Zr(Fe_{0.5}Ni_{0.5})Sb}$						
Nominal, at.%	0	33.3	0	16.7	16.7	33.3
EDX, at.%	0	33.3	0	16.7	16.7	33.3
ICP, at.%	0	33.30	0.07	16.72	16.79	32.97
Rietveld, at.%	-	33.3	-	33.3		33.3
$\mathrm{Hf(Fe_{0.5}Ni_{0.5})Sb}$						
Nominal, at.%	0	0	33.3	16.7	16.7	33.3
EDX, at.%	0	0	33.3	16.7	16.7	33.1
ICP, at.%	0	0.31	33.01	16.70	16.81	32.46
Rietveld, at.%	-	-	33.3	33.3		32.2

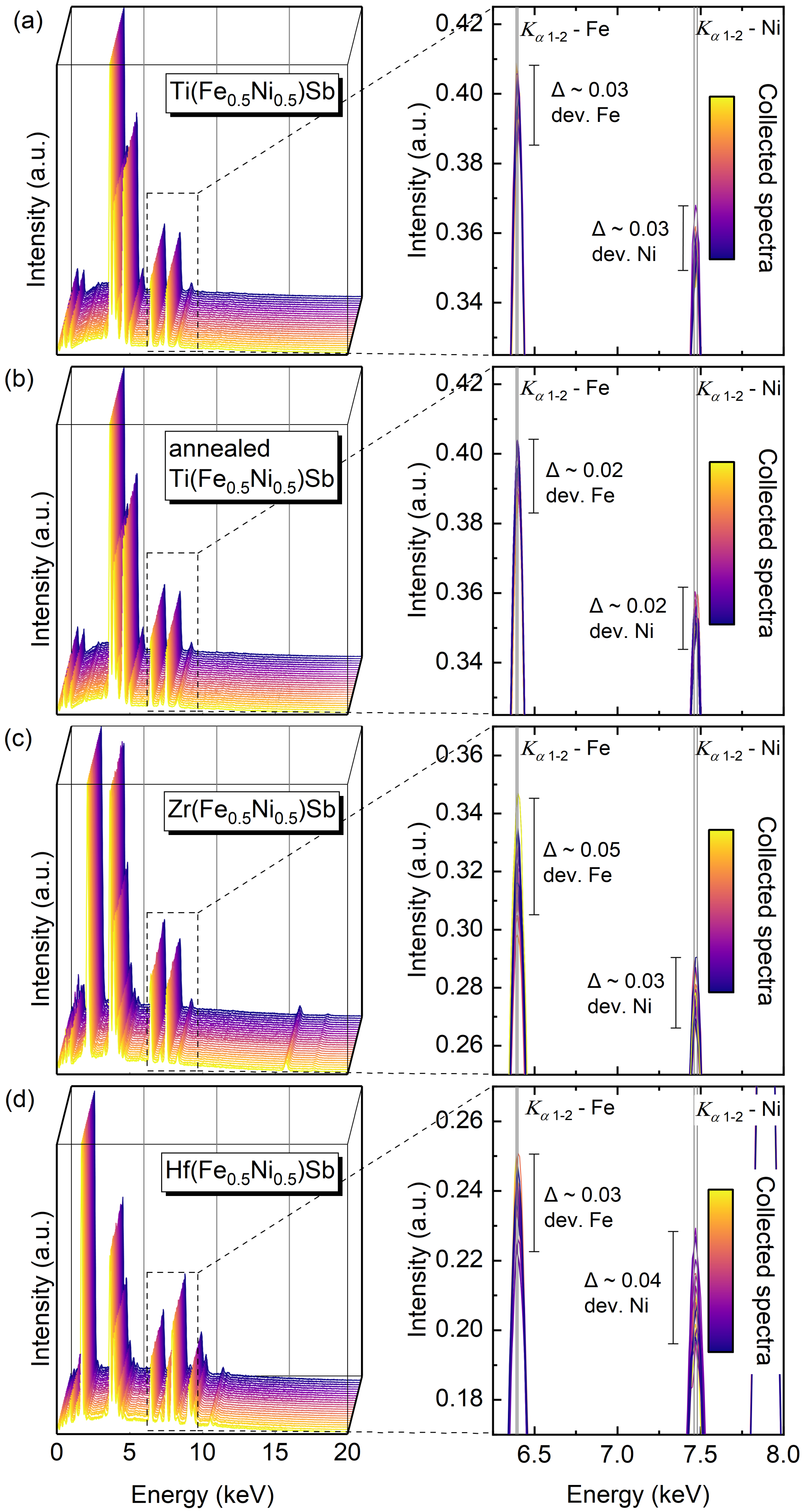

Figure S2: (a-d) Collected EDX spectra of obtained X(Fe$_{0.5}$Ni$_{0.5}$)Sb where X = Ti, Zr, or Hf samples, right panel demonstrates the deviation of $K_{\alpha 1}$ line intensities of Fe and Ni across different grains.

Rietveld refinement results

The crystal structure of obtained $X(\mathrm{Fe}_{0.5}\mathrm{Ni}_{0.5})\mathrm{Sb}$ where $X = \mathrm{Ti}$, Zr or Hf compounds was investigated by X-ray powder diffraction. All crystallographic calculations were performed with the WinCSD software[1] and presented in Table S3.

Table S3: Theoretical density d_{teor}, experimental density d_{exp}, lattice parameter a, isotropic atomic displacement parameters B_{ISO}, site occupancy factor SOF, weighted profile R-factor R_{wp}, and intensity R-factor R_p of obtained $X(\mathrm{Fe}_{0.5}\mathrm{Ni}_{0.5})\mathrm{Sb}$ where $X = \mathrm{Ti}$, Zr or Hf compounds.

Sample	d_{teor}, g cm^{-3}	d_{exp}, g cm^{-3}	a, Å	B_{ISO}			SOF			R_{wp} (%)	R_p (%)
				X	Fe, Ni	Sb	4a$_X$	4c$_{\text{Fe,Ni}}$	4b$_{\text{Sb}}$		
$\mathrm{Ti}(\mathrm{Fe}_{0.5}\mathrm{Ni}_{0.5})\mathrm{Sb}$	7.30	7.26	5.91146(3)	0.70(3)	0.55(3)	0.17(1)	1	1	1	7.3	4.4
an. $\mathrm{Ti}(\mathrm{Fe}_{0.5}\mathrm{Ni}_{0.5})\mathrm{Sb}$	7.30	7.25	5.91657(2)	1.50(2)	1.32(2)	0.785(8)	1	1	0.958(3)	5.8	3.7
$\mathrm{Zr}(\mathrm{Fe}_{0.5}\mathrm{Ni}_{0.5})\mathrm{Sb}$	7.93	7.64	6.09491(7)	0.44(3)	0.68(1)	0.25(2)	1	1	1	7.2	4.6
$\mathrm{Hf}(\mathrm{Fe}_{0.5}\mathrm{Ni}_{0.5})\mathrm{Sb}$	10.66	10.62	6.06299(5)	0.31(1)	0.79(2)	0.33(2)	1	1	0.965(2)	6.6	4.3

Modified Debye-Callaway model for lattice thermal conductivity

In the modified Debye-Callaway model[2], the lattice thermal conductivity consists of two components, $\kappa_{\text{lat}} = \kappa_1 + \kappa_2$, where

$$\kappa_1 = \frac{k_B}{2\pi^2 v_m}\left(\frac{k_B T}{\hbar}\right)^3 \int_0^{\Theta_D/T} \tau_c(x)\frac{x^4 e^x}{(e^x-1)^2}\,dx \tag{1}$$

$$\kappa_2 = \frac{k_B}{2\pi^2 v_m}\left(\frac{k_B T}{\hbar}\right)^3 \frac{\left(\int_0^{\Theta_D/T} \frac{\tau_c(x)}{\tau_N(x)}\frac{x^4 e^x}{(e^x-1)^2}\,dx\right)^2}{\int_0^{\Theta_D/T} \frac{\tau_c(x)}{\tau_N(x)\tau_{\text{ph}}(x)}\frac{x^4 e^x}{(e^x-1)^2}\,dx} \tag{2}$$

Here, $x = \frac{\hbar\omega}{k_B T}$ is dimensionless, where ω is the phonon frequency, k_B is the Boltzmann constant, $\hbar$ is the reduced Planck constant, and T is the temperature.

$$\tau_c^{-1}(x) = \tau_{ph}^{-1}(x) + \tau_N^{-1}(x) \tag{3}$$

$$\tau_{ph}^{-1}(x) = \tau_N^{-1}(x) + \tau_U^{-1}(x) + \tau_{pd}^{-1}(x) + \tau_{ph-el}^{-1}(x) \tag{4}$$

The phonon relaxation time, τ_{c}, accounts for normal phonon-phonon scattering, Umklapp processes, point defect scattering, and scattering of phonons by electrons. The overall phonon relaxation rate can be written as:

$$\tau_c = Ax^{\zeta}T^{\eta} + Bx^{\alpha}\left(\frac{T}{\theta_D}\right)^{\beta} e^{\frac{-\theta_D}{\delta T}} + Cx^4T^4 + DxT^2 \tag{5}$$

where $\zeta = 1$, $\eta = 4$, $\alpha = 2$, $\beta = 2$, and $\delta = 2$. Obtained results are shown in Table S4.

Table S4: Thermal conductivity fitting parameters

Sample	A, s^{-1}	B, s^{-1}	C	D, K^{-2}s^{-1}	Debye temperature θ_D
Ti(Fe$_{0.5}$Ni$_{0.5}$)Sb	$2.88 \cdot 10^{-4}$	$1.027 \cdot 10^{12}$	0.03	$1.79 \cdot 10^{6}$	295
an. Ti(Fe$_{0.5}$Ni$_{0.5}$)Sb	$2.38 \cdot 10^{-4}$	$1.252 \cdot 10^{12}$	0.21	$1.94 \cdot 10^{6}$	289
Zr(Fe$_{0.5}$Ni$_{0.5}$)Sb	$3.78 \cdot 10^{-5}$	$1.958 \cdot 10^{11}$	0.04	$3.90 \cdot 10^{6}$	278
Hf(Fe$_{0.5}$Ni$_{0.5}$)Sb	$6.85 \cdot 10^{-5}$	$9.241 \cdot 10^{10}$	0.23	$6.55 \cdot 10^{6}$	252

Thermoelectric efficiency

The calculated dimensionless figure of merit zT for all obtained samples is shown in Fig. S3. As presented, zT for undoped quaternary half-Heusler remains modest due to a non-optimized carrier concentration. Nevertheless, further optimization, along with controlling the formation of Sb vacancies, will be essential for rational designing n- and p-type quaternary half-Heusler thermoelectrics.

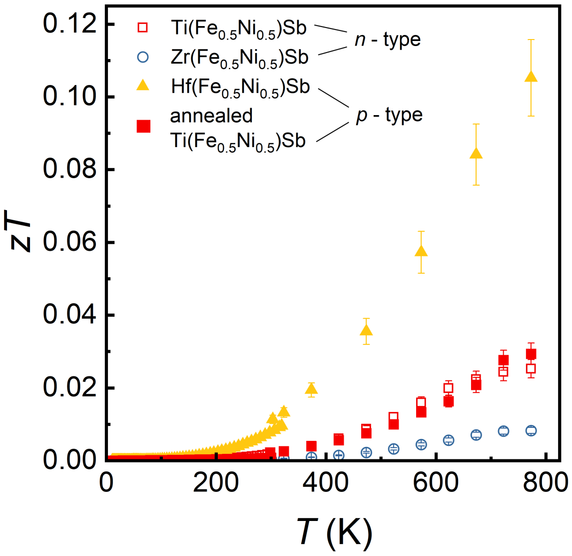

Figure S3: Calculated zT of obtained X(Fe$_{0.5}$Ni$_{0.5}$)Sb where X = Ti, Zr or Hf samples.

Phonon-drag effect

Upon analyzing the low-temperature transport properties (Fig. S4), we notice that temperature dependence of α becomes non-linear below 50 K for almost all investigated samples and can not be described by diffusive transport model[3].

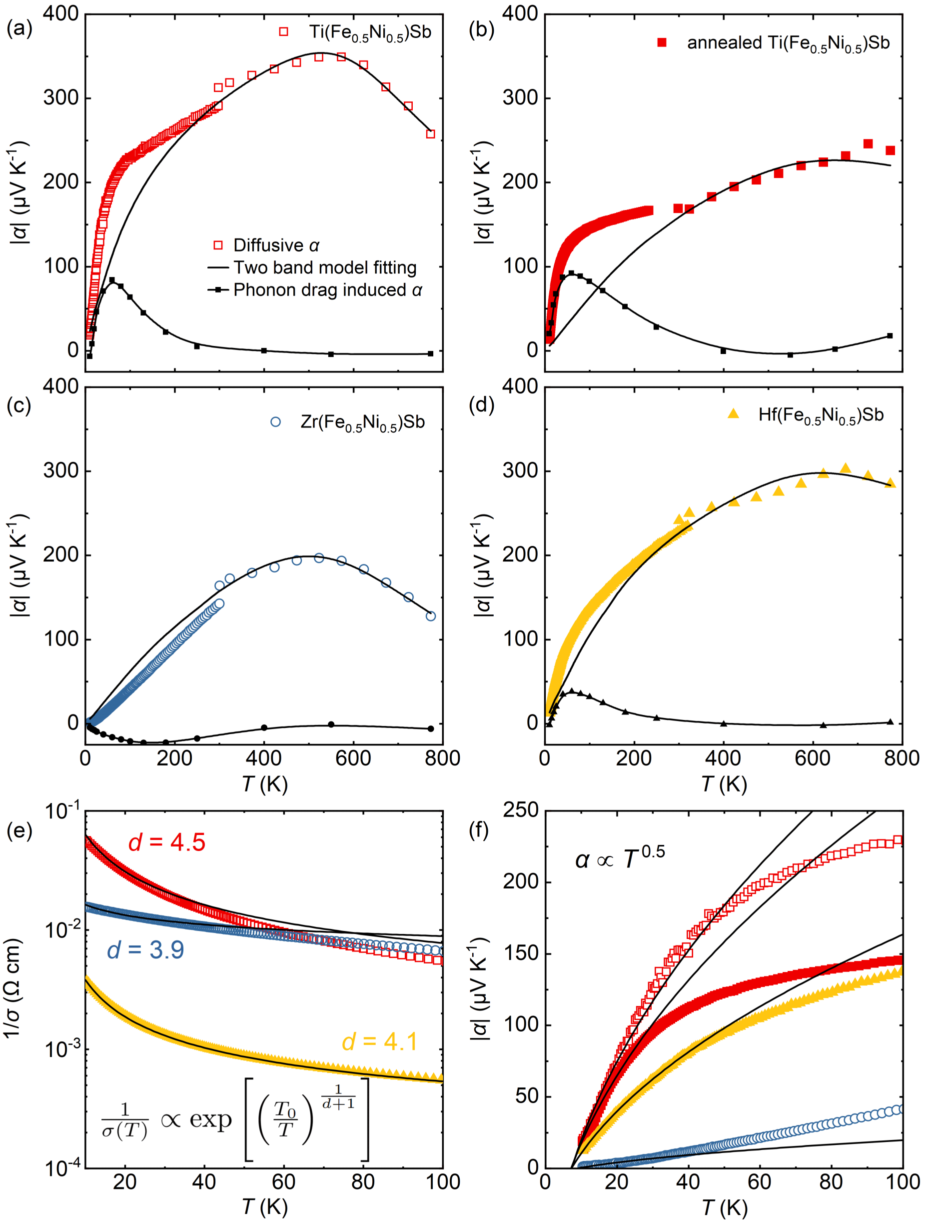

Figure S4: (a-d) Measured and two-band model fitting[3] of Seebeck coefficient of obtained $X(\mathrm{Fe}_{0.5}\mathrm{Ni}_{0.5})\mathrm{Sb}$ where X = Ti, Zr or Hf samples. (e) $1/\sigma$ vs $T^{-0.2}$ alongside with fitting by VRH. (f) Seebeck coefficient fitted by VRH localization ($\alpha \propto T^{0.5}$).

The most pronounced changes are observed in the Seebeck coefficient, which at low temperatures ($\alpha > 150$ μV K^{-1}) should follow the relation:

$$|\alpha| = -\frac{\pi^2}{3}\frac{k_B}{e}\frac{k_B T}{E_\mathrm{F}}\left(r + \frac{3}{2}\right) \tag{6}$$

where k_B is the Boltzmann constant, e is the electron charge, E_F is the Fermi energy, and r is the scattering factor

($r = -1/2$ for acoustic phonon scattering). In this case, α decreases monotonically with temperature, approaching zero at 0 K. However, plotting α/T clearly reveals a peak below 50 K (Fig. S6A). Moreover, attempts to fit the experimental data using a two-band model failed to describe low-temperature data of α (Fig. S4). Possible explanations for the observed behavior of the Seebeck coefficient include (i) magnetic or structural phase transitions, (ii) electron-electron interactions (Kondo insulators), (iii) localization of charge carriers (variable range hopping), and (iv) the phonon-drag effect.

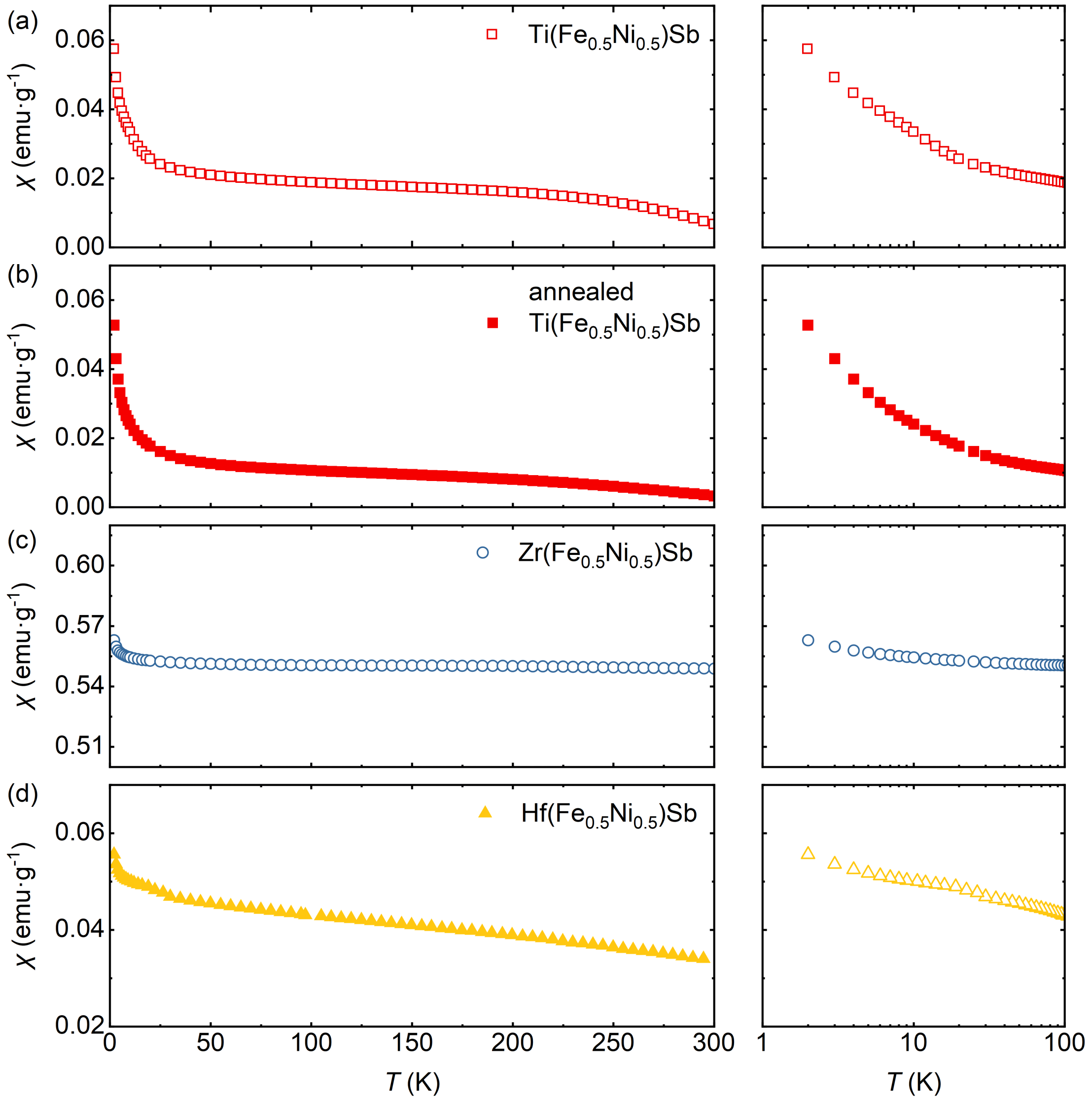

Figure S5: (a-d) Magnetic susceptibility of obtained $X(\mathrm{Fe}_{0.5}\mathrm{Ni}_{0.5})\mathrm{Sb}$ where $X =$ Ti, Zr or Hf samples, respectively.

Measurements of magnetic susceptibility (Fig.S5) revealed that none of the investigated samples exhibited a magnetic phase transition at low temperatures and indirectly suggesting the absence of structural phase transitions. To evaluate electron-electron interactions, we selected the Ti(Fe$_{0.5}$Ni$_{0.5}$)Sb sample, which exhibits the highest α/T ratio. Measurements of α, σ, and κ (Fig.S6) under magnetic fields of 0T and 7T, in the temperature range of 10K to 150K, revealed no differences, thereby excluding field dependence and, consequently, the presence of Kondo-like effects. Fitting σ and α using VRH localization failed to describe the observed low-temperature behavior, yielding physically

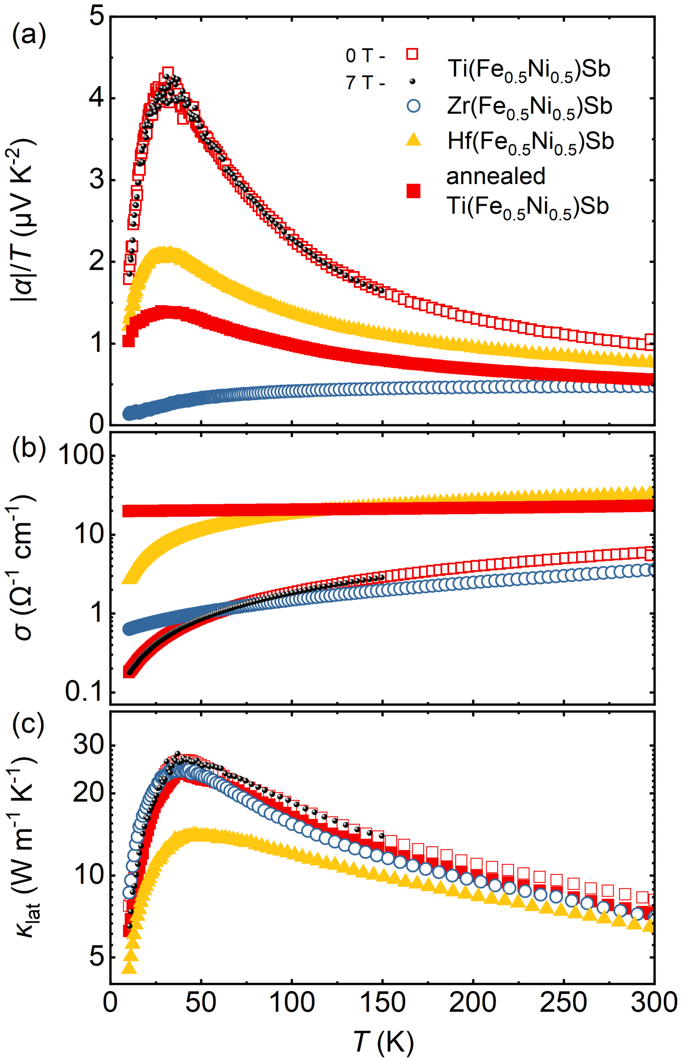

Figure S6: (a) Seebeck coefficient divided by temperature $|\alpha|/T$, (b) electrical conductivity σ (in logarithmic scale), and lattice thermal conductivity (c) κ_{lat} (in logarithmic scale) as a function of temperature of obtained X(Fe$_{0.5}$Ni$_{0.5}$)Sb where X = Ti, Zr or Hf samples.

inappropriate parameters: $T_0 > 1$, $d > 3$ for σ, and $\alpha = 0$ at 8 K.

Considering this, the phonon-drag effect appears as the last valuable explanation for the observed non-linearity of the Seebeck coefficient at low temperatures. In the phonon-drag effect, phonons most efficiently scatter electrons or holes when the scattering time is much higher than charge carriers, leading to an enhanced Seebeck coefficient. In our case, the peak in α/T matches the peak in κ_{lat}, indicating maximal phonon-electron interaction in investigated samples. This interaction adds a phonon-drag term, α_{p}, to the regularly observed diffusive term, α_{d}, resulting in the total Seebeck coefficient $\alpha = \alpha_{\text{d}} + \alpha_{\text{p}}$. At its maximum, $|\alpha_{\text{p}}| \approx 85$ μV K^{-1} at 50 K, constituting nearly 50% of the total $|\alpha|$. It is important to note that the phonon-drag effect in other materials can lead to $|\alpha| > 1000$ μV K^{-1}.[4–6] However, these materials typically exhibit much higher $\kappa_{\text{lat}} > 100$ W m^{-1}K^{-1}, which is responsible for more effective charge carrier scattering.

References

(1) Akselrud, L.; Grin, Y. WinCSD: software package for crystallographic calculations (Version 4). *Journal of Applied Crystallography* **2014**, *47*, 803–805.

(2) Glassbrenner, C. J.; Slack, G. A. Thermal Conductivity of Silicon and Germanium from 3°K to the Melting Point. *Physical Review* **1964**, *134*, A1058–A1069.

(3) Parzer, M.; Riss, A.; Garmroudi, F.; de Boor, J.; Mori, T.; Bauer, E. SeeBand: A highly efficient, interactive tool for analyzing electronic transport data. *arXiv preprint arXiv:2409.06261* **2024**,

(4) Wagner-Reetz, M.; Kasinathan, D.; Schnelle, W.; Cardoso-Gil, R.; Rosner, H.; Grin, Y.; Gille, P. Phonon-drag effect in $FeGa_3$. *Physical Review B* **2014**, *90*, 195206.

(5) Tomczak, J. M.; Haule, K.; Kotliar, G. Signatures of electronic correlations in iron silicide. *Proceedings of the National Academy of Sciences* **2012**, *109*, 3243–3246.

(6) Takahashi, H.; Okazaki, R.; Yasui, Y.; Terasaki, I. Low-temperature magnetotransport of the narrow-gap semiconductor $FeSb_2$. *Physical Review B* **2011**, *84*, 205215.